




Influence of zirconium ions on the key characteristics of V₂O₅ nanorods and current–voltage features of the n-Zr_xV₂O₅/p-Si photodetector

R. Thangarasu^{1,*}, K. Kulathuraan², J. H. Chang³, S. Subramani⁴, N. Rajiv Chandar⁵, O. N. Balasundaram¹, K. Mohanraj³, Mohd. Shkir^{6,7,*} , and Atif Mossad Ali^{6,8}

¹Department of Physics, PSG College of Arts & Science, Coimbatore, Tamil Nadu 641 014, India

²Department of Physics, Arulmigu Palaniandavar College of Arts and Culture, Dindigul Road, Palani 624601, India

³Department of Environmental Engineering and Management, Chaoyang University of Technology, 168 Jifeng E. Rd., Wufeng District, Taichung 41349, Taiwan

⁴Department of Electronics, PSG College of Arts & Science, Coimbatore, Tamil Nadu 641 014, India

⁵Department of Physics, Coimbatore Institute of Technology, Coimbatore, Tamil Nadu 641 014, India

⁶Department of Physics, Faculty of Science, King Khalid University, Abha, Saudi Arabia

⁷School of Science and Technology, Glocal University, Saharanpur, Uttar Pradesh 247001, India

⁸Department of Physics, Faculty of Science, Assiut University, Assiut 71516, Egypt

Received: 1 August 2021

Accepted: 27 November 2021

Published online:

7 January 2022

© The Author(s), under exclusive licence to Springer Science+Business Media, LLC, part of Springer Nature 2022

ABSTRACT

This article reports microstructural, morphological, optical, and photoresponse characteristics of pure and zirconium-doped V₂O₅ nanorods (Zr:V₂O₅; Zr at. 1, 3, 5, and 7 wt%) that were synthesized via the wet precipitation method. Undoubtedly, under experimental conditions, a growth mechanism has been proposed which explains morphological evolution. The microstructural analysis confirmed that the prepared samples showed a broad peak consistent with the V₂O₅ orthorhombic structure, and the absences of other reflections in this pattern ensure the phase purity. The optimized average crystallite size is determined by using Scherrer's equation from the most influential (002) peak of diffraction, which has coincided with those calculated by the TEM micrograph. SEM images showed agglomerated particles on the surfaces owing to an increase in the Zr-doping levels. The outcomes of Raman and XPS indicate that Zr doping can facilitate the generation of V⁵⁺ and oxygen vacancy. The recorded UV-DRS spectra reveal the redshifts, and the estimated optical bandgap (E_g) was decreasing with increasing Zr amount, which is further confirmed by PL studies. We used the nebulizer spray technique, a cost-effective, sophisticated, and effective way to formulate an n-Zr_xV₂O₅/p-Si photodetector. The formulated n-Zr_xV₂O₅/p-Si photodetector has good photoconducting behavior.

Address correspondence to E-mail: thangarasu1987@gmail.com; shkirphysics@gmail.com

1 Introduction

The synthesis of inorganic nanostructured semiconductor materials has fascinated researchers because of their considerable physical/chemical properties, which turn in recent years from their compared with the bulk to the nanoscale range [1]. Due to their versatile structures, semiconductor nanostructures serve as one of the most powerful nanoscience platforms today. Therefore, the design and synthetic realization of complex oxide nanorods with predictable physical properties are of paramount importance for advancing fundamental and applied research in this area. Because of their particular physical and chemical properties, group II–VI materials are considerably significant for all semiconductors. Vanadium is a transition metal that is semiconducting and can form several oxides. The type V_2O_5 is the most stable at ambient temperature and oxygen potential. It is a solid stoichiometric oxide, where the oxidation state of vanadium is + 5. In through the lowering partial pressure of O_2 , vanadium's valence varies significantly, allowing the production of a family of stoichiometric oxides: V_2O_4 , V_3O_5 , V_4O_7 , VO , VO_2 , and V_2O_3 has recently been found to be able to form several non-stoichiometric oxygenated compounds [2] as well. In the material of V_2O_5 is thus growing more likely to be researched and for future applications used in industry such as [3], Li+ battery cathodes [4], electrical and optical switching devices [5], and solar cells [6], etc. Most studies rely on the bottom-up synthesis of V_2O_5 nanoparticles by many techniques such as soft base, hydrothermal, pulsed ablation of the laser, and so on [7]. Wet chemical precipitation among these techniques is a low cost, environmentally sustainable approach to the processing of materials in different nano-architectures. Although doping with various metallic elements of the base metal oxide, for example, noble metals and transition metal-based oxides have also been proven effective for this scope. Nonetheless, intrinsic semiconductors are commonly studied in their doped form; with dopant aid [8, 9], they can be easily modified owing to their physical/chemical characteristics. The crystal phase of the nano-dimensional semiconductors still plays a critical role. Without altering this, integrating the dopant ion into these is known as one of the research's key thrust fields. Although the dopant ions have similar characteristics, including charge, ionic radius, reactivity,

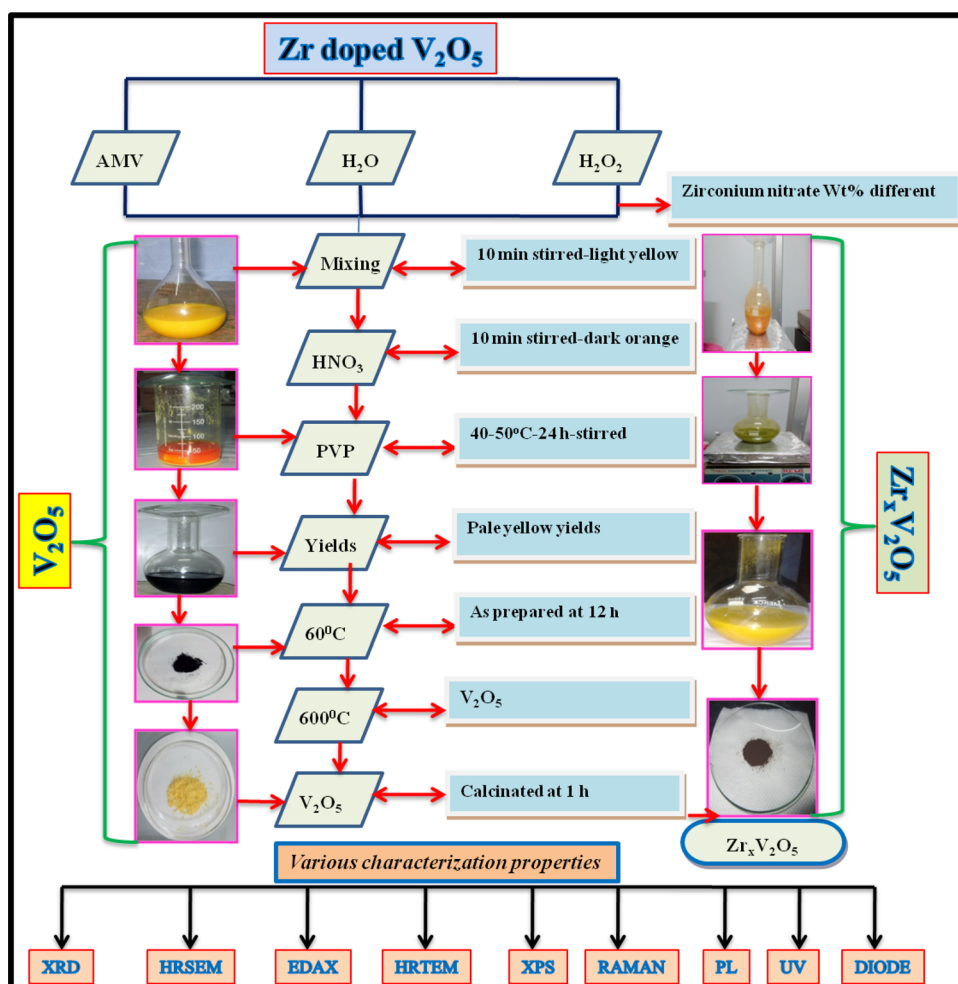
and so on, compared to the host, efficient dopant integration into the host lattice is minimal. Identifying the optimal dopant concentration is thus of great importance for achieving improved physical properties. Several authors have reported the effect of transition metal ions into V_2O_5 lattices. [10–14]. In this current study, Zr has been chosen as a dopant source owing to the strong, precise, ductile transition metal ion overwhelming physicochemical properties compared to the other metals. The Zr material is highly resistant to heat and oxidation, and it has been used as a hardening mediator in steel alloys. It is also being used to make various surgical equipment. Moreover, it is expected that Zr doping into V_2O_5 may manipulate the defect environment in the host material. In this work, systematic attempts were made to synthesize nanoparticles of pure and $Zr_x-V_2O_5$ ($x = 1, 3, 5$ and 7 wt%) with specific concentrations of dopants using the wet chemical precipitation method. The microstructural, morphological, and electrical characteristics of prepared samples were also studied in Zr doping. The n- $Zr_x-V_2O_5$ /p-Si photodetector was prepared using a nebulizer spray pyrolysis technique.

2 Experimental procedures

2.1 Pure and $Zr_xV_2O_5$ nanoparticles preparations

Zr-doped V_2O_5 samples with different doping levels were prepared, as shown in Fig. 1, via the wet chemical precipitation method. Experimental procedure: Various concentrations of Zr modified V_2O_5 nanoparticles and calcination method. In this process, ammonium metavanadate (NH_4VO_3) (ACS reagent, $\geq 99.0\%$), zirconium nitrate ($Zr(NO_3)_2$) (99% purity), hydrogen peroxide (H_2O_2) (30% (w/v), stabilized pure), polyvinylpyrrolidone k-30 (PVP) ($\geq 99.0\%$ purity), and nitric acid (HNO_3) (ACS reagent, $\geq 99.0\%$) were used as raw materials. The required amount of $4.2\text{ g } NH_4VO_3$ and $Zr(NO_3)_2$ were dissolved with deionized water to form a solution at ambient temperature were magnetic stirrer, after 10 ml of H_2O_2 was mixed in dropwise to the solution to create an homogeneously in the solution. During the process, the mixture of the solution is attained a pale yellow color. Subsequently, a few drops of HNO_3 are further added to the solution

Fig. 1 The schematic diagram of pure and $\text{Zr}_x\text{V}_2\text{O}_5$ nanoparticles preparation



vigorous stirring until pH 7, the pale yellow color solution turned into a dark orange color. After that, the capping agent of PVP is mixed to the prepared solution and stirred at 40–50 °C for 24 h. Then, the obtained precipitate was filtered and rinsed few times with DI water, and the obtained nanoparticles were dried overnight at 60 °C. Finally, it is calcinated at 600 °C for 1 h and attained yellow color ZrV_2O_5 nanoparticles. A similar way was followed for the formulation of pure V_2O_5 , without adding the zirconium nitrate.

2.2 Possible growth mechanism of V_2O_5 nanostructures

Various morphologies of the mechanism of formation of V_2O_5 nanoparticles are drawn, and their schematic representation is shown in Fig. 2. The pure V_2O_5 nanorods form a bundle shape nanorods arrangement, as shown in the illustration. Petkov et al. [15]

had previously suggested a novel approach for explaining the routes of $\text{V}_2\text{O}_5\cdot\text{H}_2\text{O}$ nanofibers. Weijie and his coworkers [16] have recently been narrating the development of disorderly V_2O_5 nanowires. They, too, believed that this process would work well with V_2O_5 nanorods. As a result, the morphology of V_2O_5 nanorods can only be due to the impact of the PVP capping agent. The monomers are adsorbed on ideal planes during particle formation in this situation, changing the tumor kinetics. Moreover, the nucleation stage may have retarded development in all preferred directions to create morphology-shaped nanorods. The regular $[\text{NH}_4\text{VO}_3]$ was precipitated in the natural solution and the simultaneous development of $[\text{H}_2\text{V}_{10}\text{O}_{28}]^{4-}$ [17, 18] during the synthetic phase. The simple corresponding chemical reactions can be stated as follows Eq. (1–5) [19],

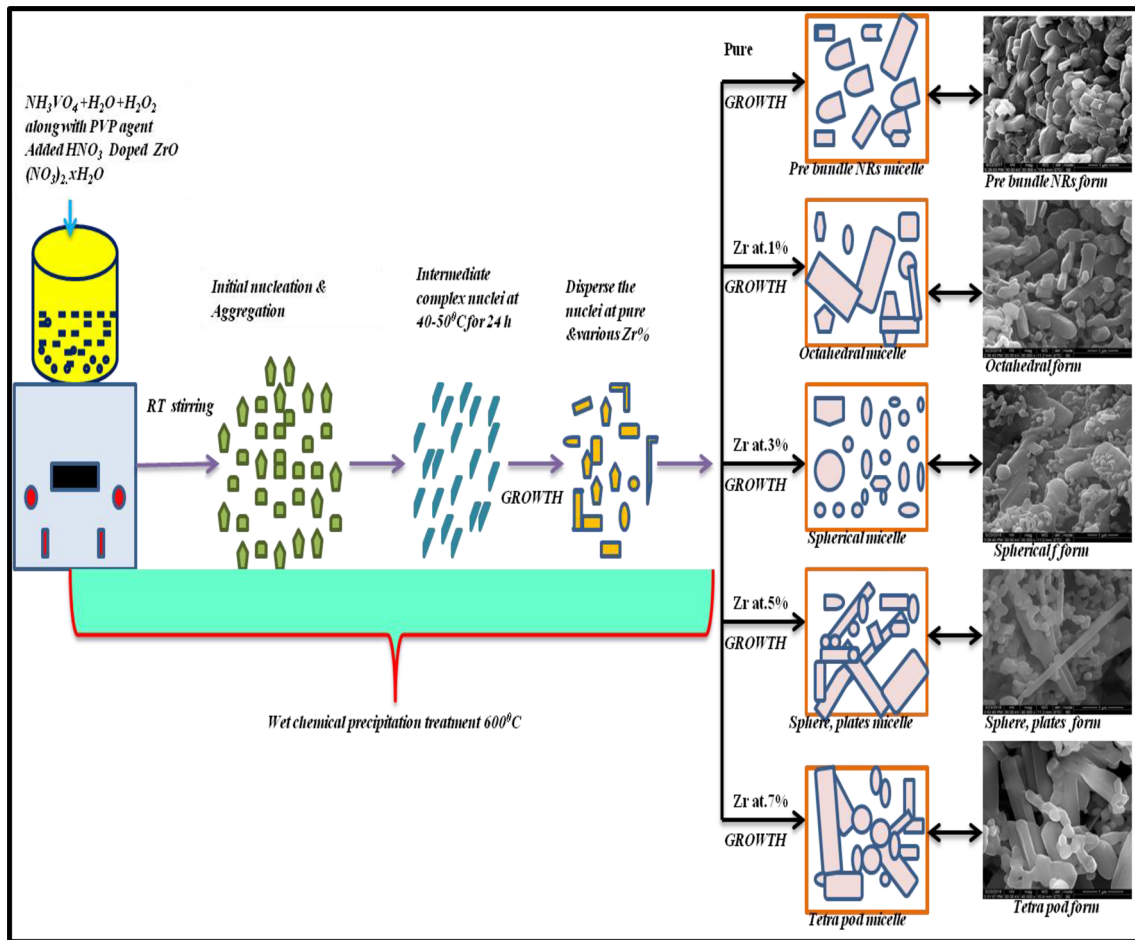
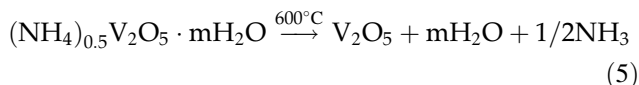
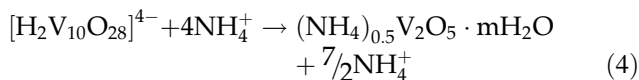
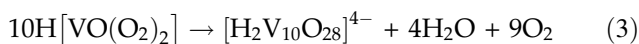
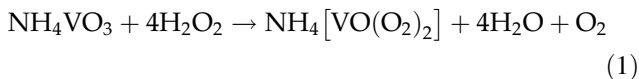
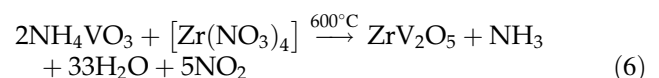


Fig. 2 The schematic representation of various morphologies formation mechanisms of $Zr_xV_2O_5$



During the reaction, the $[H_2V_{10}O_{28}]^{4-}$ ions collect in the synthetic solution in the chains formed of the PVP particles. As we learn, PVP is a kind of capping agent that hydrophobics vinyl groups use in carbonyl groups, which is the key to forming chains and their micellar formation. During the nanorods, complexes nucleate, depending on the accumulation of the $[H_2V_{10}O_{28}]^{4-}$ ions in the solution. PVP chains

form in the aqueous solution H_2O_2 , as shown in Eq. (3), at the initial phase of wet chemical treatment. In this nanorod structure are collected of the $[H_2V_{10}O_{28}]^{4-}$ ions begin to grown alongside these chains, and the novel 1-D nanorods are formed. However, a small volume of Zr^{4+} ions produced on V_2O_5 nanorods has modified growth rates and resulted in long nanorods with a small number of spherical and microdisk constructions. In the synthetic phase of Zr-doped V_2O_5 , the $[NH_4VO_3]$ was rapid in the starting solution $[H_2O_2]$ with $[Zr(NO_3)_4]$, which is the concurrent production of $[Zr(NO_3)_4]$. This uniform precursor was essential for forming a fine powder after heat treatment at $600^\circ C$ for 1 h. The simple corresponding chemical reactions can be given in Eq. (6),



The addition of a $[\text{Zr}(\text{NO}_3)_4]$ ions in the responses scheme to exceeding Eq. (3) will change the kinetics of the upcoming instrument, which is certified that the count of PVP raises the crystallinity of the samples tested and modifies the invention's morphology as shown in Fig. 2.

2.3 Characterization technique

The as-prepared nanomaterial phase constitutions are investigated by Bruker AXS D8 Advanced Discovery X-ray diffractometer using $\text{CuK}\alpha$ -007 radiation ($= 1.5406 \text{ \AA}$) X-ray source. The surface and cross-section microstructure analyses of Zr-doped V_2O_5 and pure materials are carried out using a scanning electron microscopy (JSM-6390 LV, JEOL-Japan), also equipped with energy-dispersive X-ray spectroscopy (EDS). Raman spectrometer is collected with a microscopic confocal Raman spectrometer (in via RAMHR4800) with 437 nm laser lines as the source of excitation. The surface properties and binding energy of Zr-doped V_2O_5 and pure are investigated using X-ray photoelectron spectroscopy (XPS- SSX-100) with Al $\text{K}\alpha$ (anode $h\nu = 1486.6 \text{ eV}$). The nanomaterials' optical properties have been studied using UV-visible spectrometry (Perkin Elmer Lambda 750, USA). The photoluminescence studies are performed with the Horiba Jobin Yuon Fluorolog instrument model with a range of 185–900 nm. The produced diode's current–voltage characteristics have been examined by a Keithley 6517 B meter in the dark and by calibrating (illumination intensity of 100 mWcm^{-2}) solar simulator.

3 Results and discussion

3.1 Microstructural study

Figure 3a displays the crystal structure of as-synthesized V_2O_5 with various amounts of Zr-doped V_2O_5 nanomaterials. The XRD pattern of the pure V_2O_5 and without additives of Zr-doped V_2O_5 reveals the orthorhombic phase of V_2O_5 (JCPDS card No: 41-1426) and also observes no additional peaks which imply the phase purity of V_2O_5 . The X-ray diffraction peaks presented at angles 2θ are 15.83° , 20.76° , 25.03° , 26.65° , 31.49° , 34.83° , and 41.80° which correspond to the planes (200), (001), (201), (110), (301), (310), and (002), respectively. The most intense peak has

appeared at (001) plane. Figure 3b reveals that the predominant diffraction peak positions (001) and (110) are shifted toward the left side due to increased Zr concentration. We observe that the peak position of various concentrations Zr-doped V_2O_5 is slightly shifted to a low-angle direction compared with pure V_2O_5 . It is identified that the high-intensity peak position (001) and (110) in various concentrations of Zr-doped V_2O_5 varied from pure V_2O_5 . Thus, providing evidence that Zr^{4+} is highly incorporated into the lattice of V_2O_5 . This attributes to the lattice expansion owing to the ionic radius of Zr^{4+} (0.84 \AA), which is more significant than that of pure V^{5+} (0.57 \AA). Furthermore, the full width at half maximum value of 7% Zr-doped V_2O_5 is greater than the remaining percentage of 5, 3, and 1% Zr-doped V_2O_5 . It reveals that the doping of Zr^{4+} can prevent the growth of V_2O_5 grains effectively. The average grain size (D) has been estimated from the FWHM of the peaks by the Scherrer's equation ($D = 0.89\lambda / \beta \cos\theta$).

Figure 3b shows the diffraction peaks of (001), (110), and (301) planes, and also estimated grain size and lattice parameters are described in Table 1. The lattice constant for the orthorhombic phase structure is determined by the relation $1/d_{hkl} = \sqrt{h^2/a^2 + k^2/b^2 + l^2/c^2}$ where a , b , and c are lattice parameters, also listed in Table 1. The change in lattice parameters is observed due to Zr ions.

3.2 SEM, EDS, and TEM analysis

Figure 4a–e displays SEM images of Zr-doped V_2O_5 with various amounts of dopants, along with pure V_2O_5 samples annealed for 1 h at 600°C . As shown in Fig. 4a, well-defined hexagonal V_2O_5 nanorods around $1 \mu\text{m}$ in length and other tightly packed one-dimensional nanostructures are self-assembled. In this regard, the morphology begins to change as zirconium nitrate is introduced as a doping chemical into the solution. Most interestingly, the Zr-doped V_2O_5 nanostructures' composition is gradually transforming into V^{5+} ions according to the molar ratio of Zr^{4+} ions. The SEM analysis shows that particle sizes decrease with the Zr^{4+} increase from 1, 3, 5, and 7%. As Zr^{4+} ions are added to the V^{5+} solution, the number of nucleation sites on samples increased, resulting in a higher degree of preferential orientation, exposed to reduced grain levels,

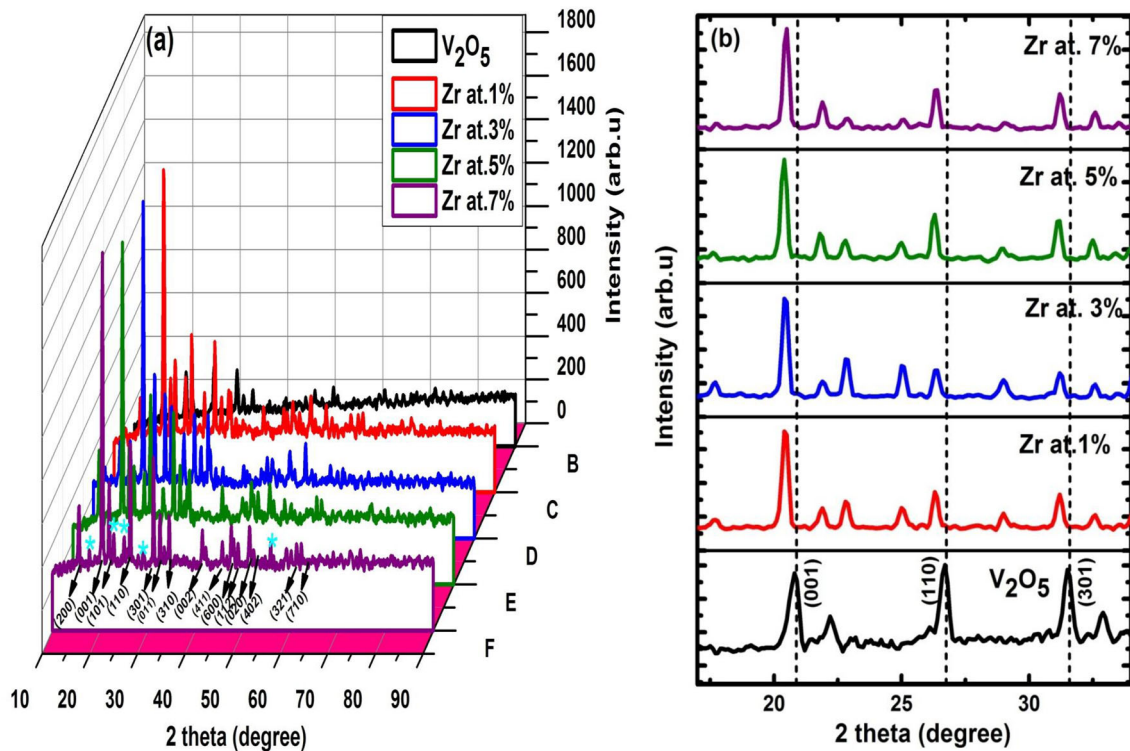


Fig. 3 **a** X-ray diffraction patterns of $\text{Zr}_x\text{V}_2\text{O}_5$ nanoparticles, **b** The $\text{Zr}_x\text{V}_2\text{O}_5$ deconvoluted XRD patterns

Table 1 Microstructural parameters of the prepared materials

$\text{Zr}_x\text{V}_2\text{O}_5$ (where $x = 0, 1, 3, 5$ and 7%)	2θ (degree)	hkl	d - spacing (nm)	FWHM (degree)	Grain size (D) nm	Dislocation density (10^{14} lines m^{-2})	Micro-strain (ε) $10^4 \text{lin}^{-2} \text{m}^{-4}$	Lattice parameters (\AA)		
								a	b	c
00	20.7631	001	4.27464	0.45970	18.3498	0.002969	0.197299	11.375	3.536	4.276
	26.6500	110	3.34224	0.38510	22.1421	0.002039	0.163507			
	31.4935	310	2.83839	0.34870	24.7230	0.001636	0.146439			
01	20.4275	001	4.34410	0.30920	27.2671	0.001345	0.132776	11.445	3.548	4.344
	26.6000	110	3.34841	0.31260	27.2746	0.001344	0.132739			
	31.1906	301	2.86526	0.28800	29.9115	0.001177	0.121038			
03	20.4312	001	4.34332	0.29460	28.6185	0.001265	0.126506	11.443	3.557	4.343
	26.3365	110	3.38131	0.29070	29.3135	0.001164	0.123507			
	31.1718	301	2.86695	0.28190	30.0463	0.001107	0.120445			
05	20.3793	001	4.35427	0.28820	29.2517	0.001169	0.123767	11.428	3.554	4.353
	26.3387	110	3.38103	0.26220	32.4993	0.000946	0.111399			
	31.1228	301	2.87135	0.28020	30.7389	0.001058	0.111778			
07	20.4664	001	4.33593	0.27590	30.5596	0.001071	0.118470	11.316	3.510	4.331
	26.2648	110	3.39037	0.25900	32.8962	0.000924	0.110055			
	31.1972	301	2.86467	0.27990	30.7776	0.001055	0.117631			

resulting in the presence of more compact, multi-faceted nanostructures. At lower content of Zr, which reveals the formation of spherical, octahedral, spheres, plates and tetrapod with the appearance of

few nanorods on their surface. The presence of nanorods can be due to Zr^{4+} being integrated into the crystal at the V^{5+} sites. Notably, as the Zr concentration decreases, the rising tetrapod is with

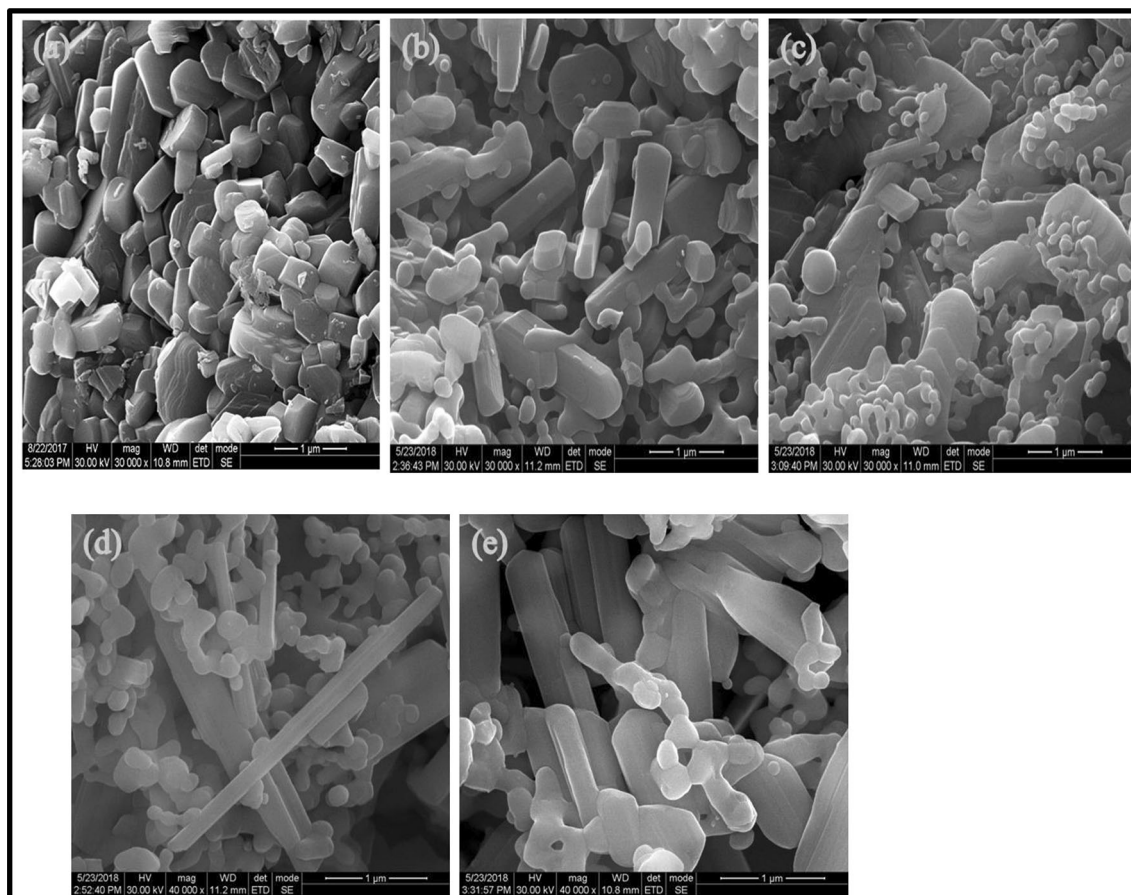


Fig. 4 a–e The SEM images of a 0, b 1, c 3, d 5, and e 7 wt% of Zr-doped V_2O_5 nanoparticles

nanorods. The observed agglomeration of nanoparticles could be attributed to the attractive forces between nanoparticles associated with the ratio of surface area to volume increased. The SEM micrographs also clearly demonstrate that the morphology on Zr doping is shifting from nanorods to tetrapods.

Nonetheless, a potential explanation for the morphology transformation of V_2O_5 from nanorods to tetrapods on Zr doping is that doping of different elements shows a significant part in altering the nanostructure measurements. However, the V_2O_5 nanorods are formed in a continuous 1-D branching and subsequent 2-D interspace filling phase and their V_2O_5 semiconductor classification. It is characteristic that polar surfaces can induce asymmetric growth, resulting in the development of specific nanostructures. EDS research revealed that in the case of Zr-doped V_2O_5 powders, all samples possess only as just elements V, O, and Zr. The atomic percentage composition results were extracted with EDS and are reported as shown in Fig. 5 inset table, where it can

be appreciated that the $Zr/(Zr + V^{5+})$ ratio is quite similar to the stoichiometry of the doping fraction as expected for each sample. The morphological evaluation of studied samples was also investigated by TEM analysis. The bright-field micrographs of TEM and HR-TEM of a descriptive set of the studied samples, as well as inset SAED pattern, are shown in Fig. 6a–e. In Fig. 6a, the sample for undoped V_2O_5 consists of single crystalline nanoparticles that can nearly be monodispersed by acidifying nitric acid-related particles suspension, which is attributed to the double-layer repulsion phenomenon and is considered responsible for the durability of colloidal systems [20, 21]. Therefore, a large number of small dispersed crystals are included in the sampling; the SAED images consist of well-structured continuous light diffraction bowls that can be counted, following XRD overhead reflection from the inside to the outside of the (001), (110), (200), and (301) orthorhombic V_2O_5 planes. For the Zr-doped samples, similar microstructures were observed, as seen in Fig. 6b–e.

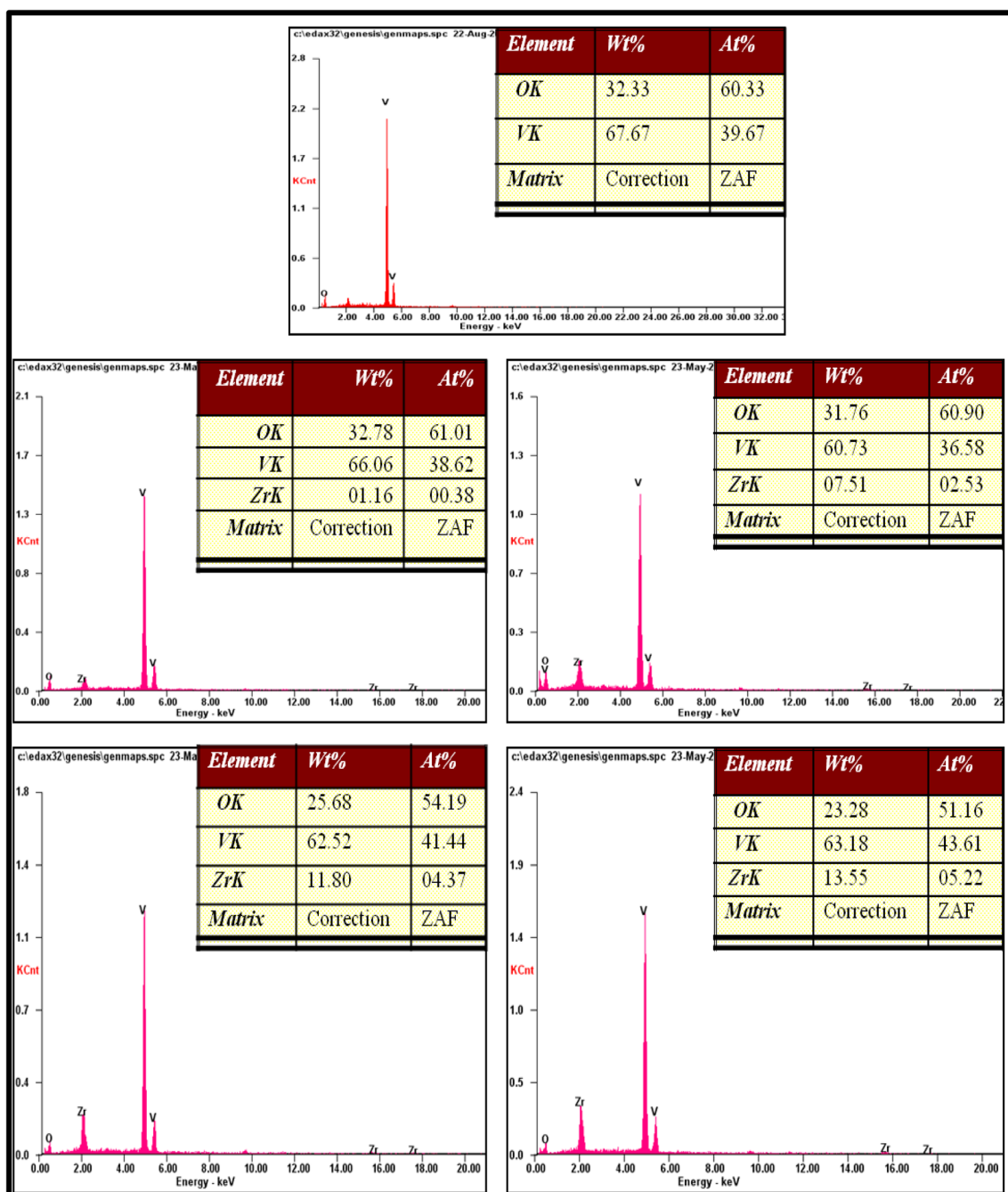


Fig. 5 a–e The EDS spectra of a 0, b 1, c 3, d 5, and e 7 wt% of Zr-doped V₂O₅ nanoparticles

Examination of the TEM and HR-TEM results reveals that Zr-doped materials exhibit identical spheroidal-like morphologies as observed for the V₂O₅, with particle sizes still adopting a lognormal distribution of mean values from 3.59 ± 0.71 nm to 4.06 ± 0.96 . Likewise, the crystalline planes can be observed, and we have their interplanar distances from the radius of electron diffraction spots shown at the SAED. The

lengths obtained (see Table 1) are entirely consistent with V₂O₅'s orthorhombic structure, demonstrating again that unnecessary phases are not separated during the synthesis of nanoparticles.

3.3 Raman spectroscopy

The Raman scattering was also performed for the crystal symmetry, structural defects, and vibrational

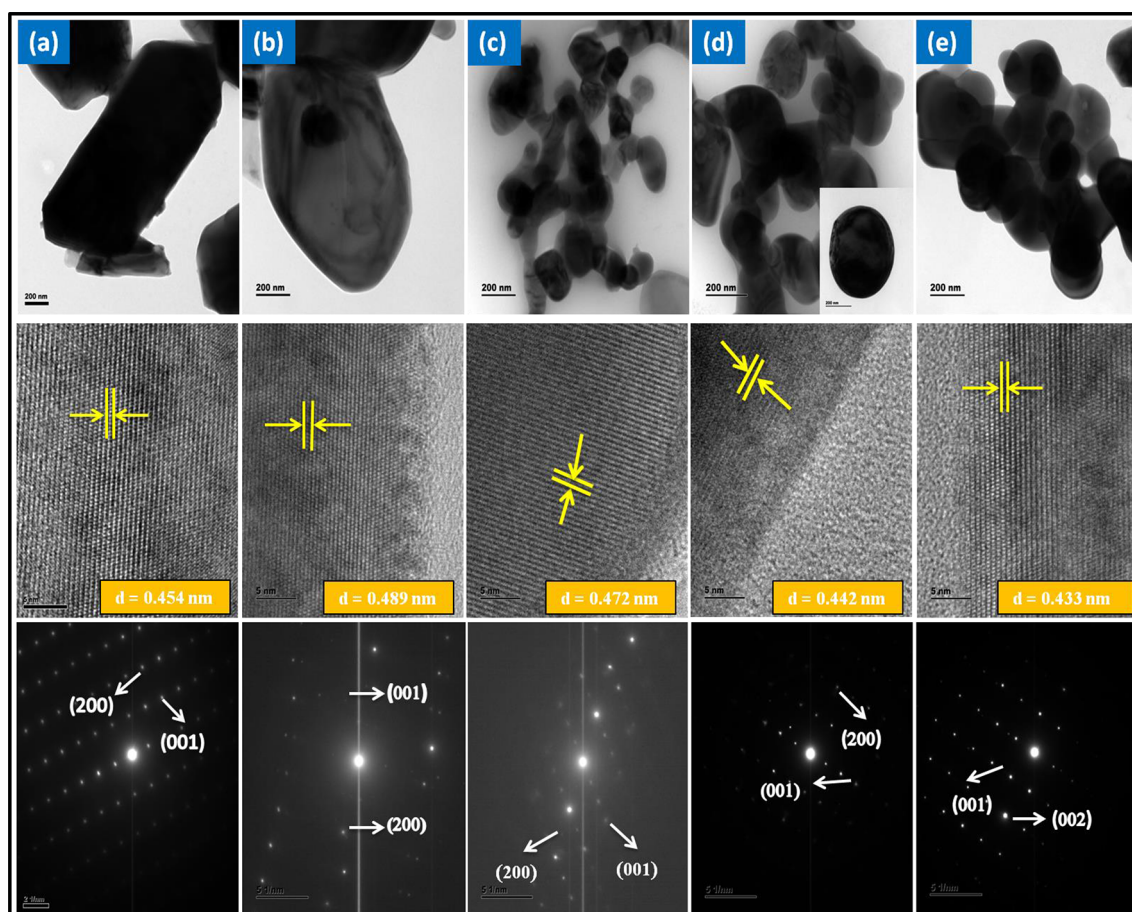


Fig. 6 a–e The TEM images of a 0, b 1, c 3, d 5, and e 7 wt% of Zr-doped V_2O_5 nanoparticles

properties of the studied samples, and the typical Raman room temperature spectrum of V_2O_5 and Zr-doped V_2O_5 samples with various concentrations is shown in Fig. 7a. All of the examined samples were exhibited in the characteristic orthorhombic structured V_2O_5 Raman spectra [22]. The Raman mode's external lower frequency range at 146 and 191 cm^{-1} corresponds to the relative motions of V_2O_5 layers concerning each other [23]. Such peaks are appeared at 146 cm^{-1} and 191 cm^{-1} , are closely correlated with the layered system, and occur only when structural order is extended. The layer-like structure of V_2O_5 is observed outside the skeleton bent mode based at 147 cm^{-1} [24]. The $V=OV$ bonds' bending vibration owing to the vibration bending of the O_3-V-O_4 bond (A_g and B_{2g} modes) is allocated for both peaks in this range, which are 283 and 404 cm^{-1} . The band located at 406 was indicated to the bending of the $V-O_4-V$ bond (A_g mode), the stretching of the $V-O_4$ bond (A_g mode), and the stretching vibration of $V-O_2$ bond (B_{2g} and B_{3g} mode), respectively. The

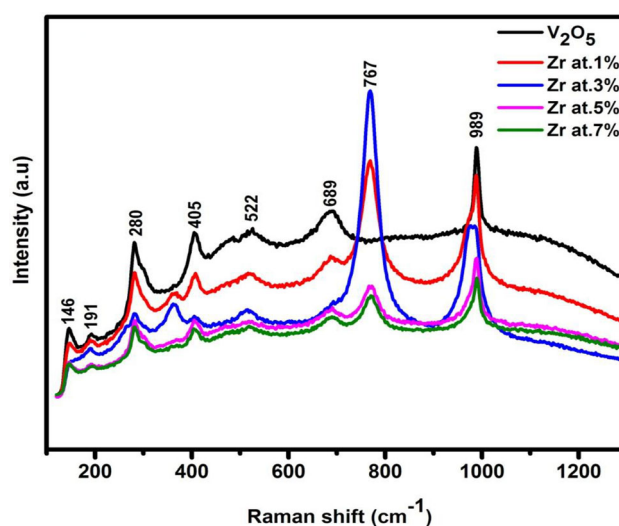


Fig. 7 The room temperature Raman spectra of pure and Zr-doped V_2O_5 nanoparticles

triply coordinated oxygen (V_3-O_C) stretching mode, which results from edged-shared oxygen atoms

common to three pyramids, is assigned to the peak at 529 cm^{-1} . The band on 689 cm^{-1} is owing to vanadium atoms' coordination with the three oxygen atoms [25]. The doubly coordinated oxygen ($\text{V}_2\text{-O}_\text{B}$) stretching mode, which results from corner-shared oxygen common to two pyramids, is attributed to the peak at 767 cm^{-1} . The band at 989 cm^{-1} , on the other hand, is further evidence of the presence of a V_2O_5 layer structure, which corresponds to vanadium bound to an unshared oxygen atom (V=O). Based on the above findings, the $\text{Zr}_x\text{V}_2\text{O}_5$ Raman spectrum displays the usual orthorhombic V_2O_5 V–O vibration. Furthermore, the Zr–O-doped samples, which could be caused by doping Zr into V^{5+} grids, do neither reveal Raman bands that correspond to the Zr–O vibration. Further, the obtained peaks shifted slightly toward higher values of the wavenumber, and the small shift suggests that the Zr incorporation of V_2O_5 lattice.

3.4 XPS study

The electronic/chemical states of pure and $\text{Zr}_x\text{V}_2\text{O}_5$ ($x = 7\%$) samples on the compositional elements were also carried out in the XPS analysis, and the characteristic spectra are revealed in Fig. 8a–d. The survey spectra of the prepared materials and index peaks studied in Fig. 8a are similar to those for the V, O, Zr, and C elements, where the binding energies are measured by taking the carbon C1s peak (284.6 eV) shown in Fig. 8b. The result of the deconvolution spectrum for V_2O_5 (Fig. 8c) displays that the doublet spectral lines of $\text{V}2p$ are detected at the binding energy of 524.47 eV ($\text{V}2p_{1/2}$) and 517.04 eV ($\text{V}2p_{3/2}$), which are specific to V^{5+} oxidation states and confirms the formation of V_2O_5 [26]. Additionally, the $\text{Zr}_x\text{V}_2\text{O}_5$ ($x = 7\%$) sample exhibit that the peak appeared at 183 and 185 eV is situated with the BE of $\text{Zr}3d_{5/2}$ and $\text{Zr}3d_{3/2}$, respectively, as shown in Fig. 8d, representing the peaks of Zr^{4+} ions [27]. The figure also states that the O 1s value is not entirely symmetric (Fig. 8d). The O1s unit, however, is divided into two parts. The O^{2-} condition is correlated to the terminal oxygen ($=\text{O}$) and the linkage oxygen ($-\text{O}-$). This peak-fitted, which around to be 533 eV is believed to approach from the various sources and it perhaps comes from originating OH groups or since the ambient humidity. Also, O^{2-} ions in the V_2O_5 orthorhombic structure are given the dominant summit at $530.1 \pm 0.2\text{ eV}$ (O_a). At the height of

$531.2 \pm 0.2\text{ eV}$ (O_b), the media binding energy portion is due to the lost O^{2-} ions inside the Matrix V_2O_5 in oxygen-deficient areas (oxygen vacancies). The amount of oxygen bonded to the V^{5+} (O_a) can be calculated using the area ratio of $[\text{O}_\text{a}/(\text{O}_\text{b}+\text{O}_\text{a})]$, which is 22.4% for the $\text{Zr}_x\text{V}_2\text{O}_5$ where $x = 7\%$; it should be noticed and maybe that there are a lot of oxygen vacancies in $\text{Zr}_x\text{V}_2\text{O}_5$ samples.

3.5 Optical properties

By evaluating their diffuse reflectance R at ambient temperature, the studied samples' optical characterization was performed. Figure 9a presents the diffused reflectance plots for undoped and Zr-doped V_2O_5 samples, and it is clear that the substitution of Zr dopants into the host V_2O_5 leads to the increase of the diffused reflectance.

The optical bandgap (E_g) energies of the investigated samples were estimated by plotting the function $f_{\text{KM}} = (F_{\text{KM}}/h\nu)^2$ vs. $h\nu$ (Taucplot), where ' h ' stands for Planck's constant and ν stands for the radiation frequency and extrapolating the linear portion of the curve to zero absorption. The plots of $(\alpha h\nu)^2$ vs. $h\nu$ for all the studied samples, as shown in Fig. 9b, and the bandgap have been obtained by extrapolating the straight-line portion of the $(\alpha h\nu)^2$ vs $h\nu$ graph. According to Tauc's plot, the estimated values of E_g for pure and $\text{Zr}_x\text{V}_2\text{O}_5$ are about 2.20 , 2.38 , 2.34 , 2.30 , and 2.26 eV , respectively. The undoped V_2O_5 sample's optical bandgap was measured to be 2.20 eV , which is 0.12 eV blue-shifted compared to the bulk value of V_2O_5 (2.65 eV). They may notice while this blue shift could be obtained by the phenomena of quantitative containment linked to the nanosized crystallite samples [28]. In Fig. 9b, it could be shown that the Zr incorporation causes a significant decrease in bandgap when compared to the pure V_2O_5 sample, which indicates the presence of defects in atomic structure disorder in V^{5+} during Zr^{4+} doping.

3.6 Photoluminescence

Figure 10a shows PL spectra of pure samples and $\text{Zr}_x\text{V}_2\text{O}_5$ samples were examined at room temperature with specific dopant concentration Zr. One peak is at 418 nm (2.96 eV), followed by an extreme blue emission at 440 nm (2.81 eV) and a significant visible emission at 549.2 nm (2.26 eV). It is possible to note that Zr-doped samples' emission spectra were

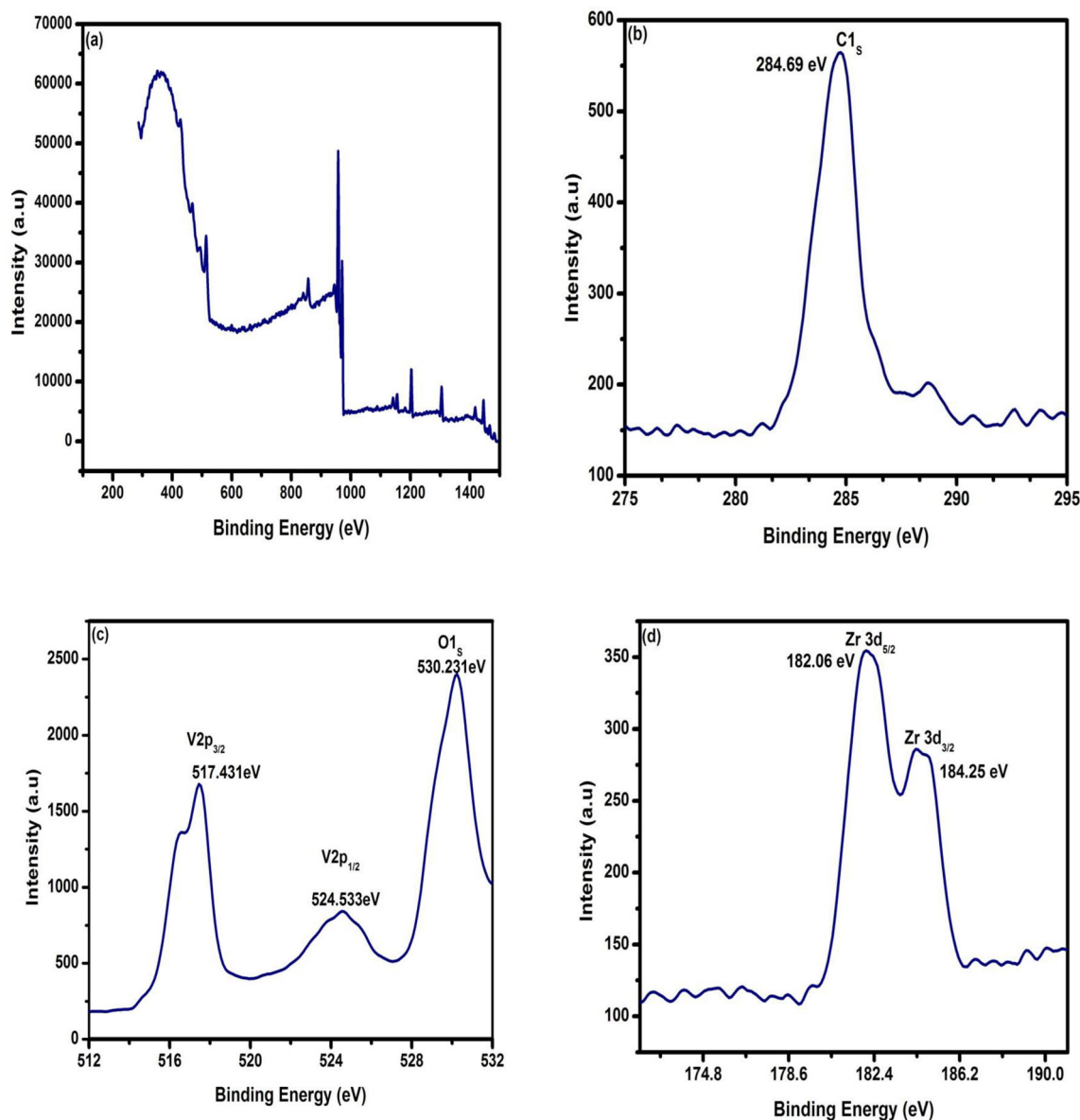


Fig. 8 a XPS survey spectrum and deconvoluted spectra of **b** C 1s, **c** V 2p and O 1s, and **d** Zr 3d region of 7 wt% Zr-doped V_2O_5 nanoparticles

extended with three dominant maximums spanning the entire visible region. The UV and visible peaks in V_2O_5 's PL spectrum are well known [29]. The exciton recombination corresponding to the near-band edge excitation emission of the small bandgap V_2O_5 , namely the recombination of free and excited by an excision collision mechanism, can be induced by defects such as the interface of a trap at the grain boundaries. It originates from the exciton recombination corresponding to the near-band edge excitation emission of the broad bandgap V_2O_5 . The self-trapped excitons' radiative recombination loop

arising from the excited charge-transfer state of the V_2O_5 species can be traced to the blue-green emission band centered at 453 nm. They also blamed the samples' high density of surface defects, such as oxygen vacancies, vanadium vacancies, oxygen interstitials, and vanadium interstitials, on the high density of surface defects. This indicates that the electron is migrating from the ionized oxygen vacancies to the valance band point. Because of the recombined emission of the lowest split-off V 3d band to the O 2p valance band, the high visible emission peak is at 550 nm [30]. The Zr^{4+} -doped V^{5+} lattice's

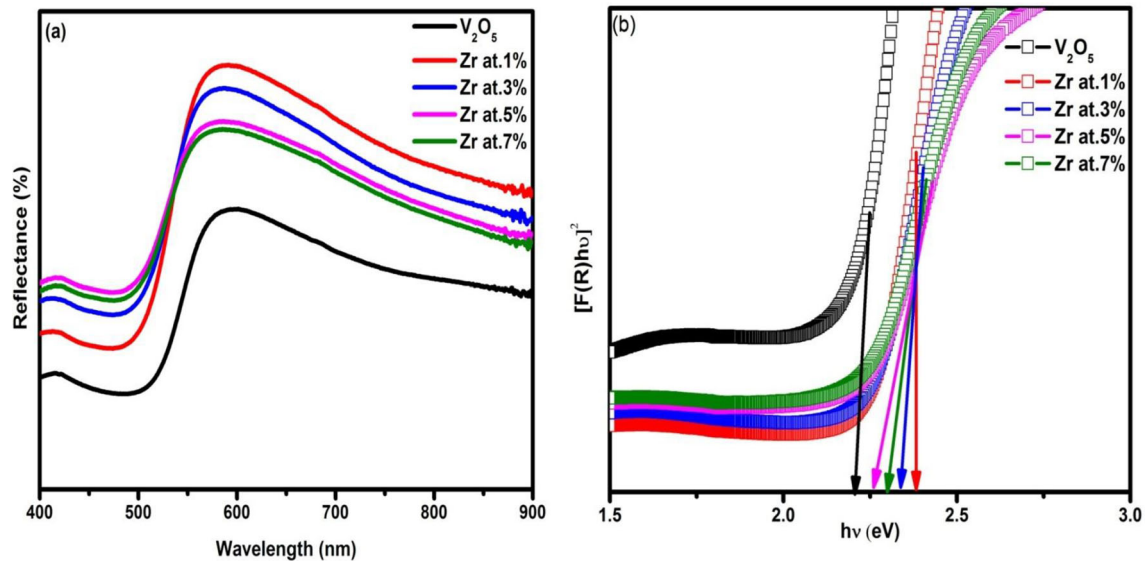


Fig. 9 **a** The UV reflectance spectra of pure and Zr-doped V_2O_5 nanoparticles, **b** The plots of $(\alpha hv)^2$ vs. $h\nu$ of pure and Zr-doped V_2O_5 nanoparticles

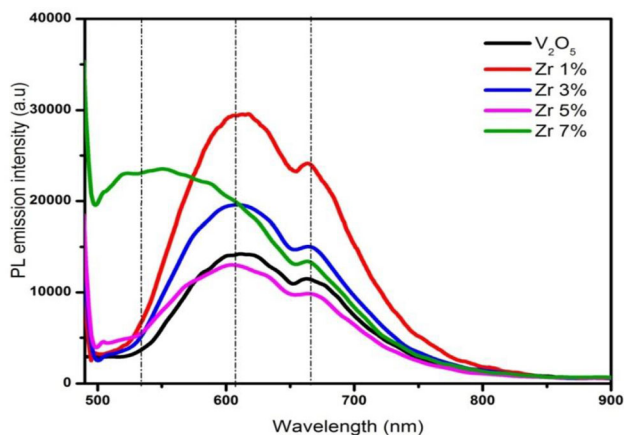


Fig. 10 The room temperature PL spectra of pure and Zr-doped V_2O_5 nanoparticles

emission wavelengths do not vary with changing Zr^{4+} ions' impurity, but the doped samples' relative intensities are varied. For the concentration of 1% at Zr^{4+} , the relative fluorescence intensity is highest and nearly twice that of the undoped sample. This could lower the surface-to-volume ratio, resulting in fewer surface defects as doping concentrations decreased. Furthermore, an increase in Zr^{4+} concentration reduces the strength of PL pollution by 3, 5, and 7%, respectively. In the samples currently being analyzed,

this decrease in PL strength may be caused by various non-radiative recombination processes [31].

3.7 Fabrication and characterization of $n-Zr_xV_2O_5/p$ -Si diodes

The device configuration for making diodes is shown in Fig. 11. The semiconductor used in this investigation was single-crystal silicon p-type with 600 μm thickness and 5–10 Ωcm resistivity. Firstly, the silicon p-type single crystal has been cleaned. The wafer was etched by HF to remove the native oxide on the p-Si surface and then rinsed for 10–15 min in deionized water using an ultrasonic bath and finally washed chemically using a method on successive baths of methanol and acetone. After the cleaning process, pure and doped samples in colloidal form were coated on p-type silicon by the nebulizer spray coating method. The films were then dried on a hot plate at 150 $^{\circ}C$ for 10 min to evaporate the solvent and eliminate organic residues. The ohmic contact was prepared to apply the front and back surface of the p-Si wafer with high purity of Ag paste, and then, it is annealed for 5 min at 90 $^{\circ}C$.

Figure 11 shows dark and illumination i–v characteristics at atmospheric temperature of $n-V_2O_5/p$ -Si

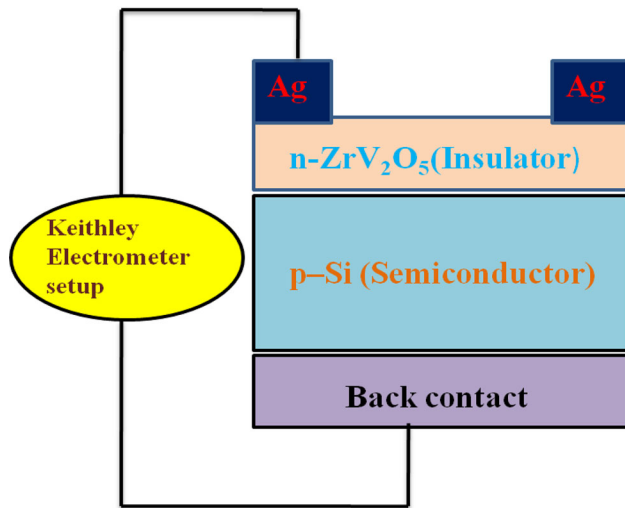


Fig. 11 The schematic representation of n-Zr_xV₂O₅/p-Si diode

and n-Zr_xV₂O₅/p-Si junction diodes. All *I*–*V* elements in the figure show the asymmetrical and not ohmic activity in the dark condition. The increase in the forward current is caused by the change in lighting conditions for photogenerated carriers. As a result, when the diodes are illuminated at a given applied voltage, the reverse current is higher than when they are dark. This is one that you might use. Due to the photo-excitation of the charging carriers from the valance band, the voltage dependency of the reverse current can be attributed to a defect-perturbed host state (*V_b*). After illumination of a diode, electron–hole pairs are formed in the depletion region due to photon absorption with greater photo-energy than the bandgap of semiconducting materials. This roll progression leads to photocurrent production alongside the reverse bias-direction. It is found that the pure and doped diodes demonstrate the well-rectifying activity with lighting. The forward current reaction of n-Zr_xV₂O₅/p-Si diodes concerning Zr⁴⁺ concentration is depicted in Fig. 12a–e. As a result, the increase in forward current with Zr⁴⁺ dopant is due to an increase in carrier concentration, which results in the energy band bending and a narrowing of the depletion field. The forward- and reverse-biased semi-log (*J*–*V*) characteristics of the diodes developed in dark conditions are shown in Fig. 12f–h. The *J*–*V* curves typically provide details about the junction properties such as the correction ratio (RR), the series and shunt resistances (*R_s* and *R_{sh}*), the reverse saturation current (*I_s*), and the factor of ideality (*n*). Additionally, the *J*–*V* characteristics

were used to investigate the diodes' conduction mechanism. Indeed, the *J*–*V* curve's exponential manner depends on the property characteristic of the active materials used for the diodes. In the exponential region, the slope of the *J*–*V* features depends on two main parameters, that is, factor ideality (*n*) and reverse current saturation (*I_s*). The ideality aspect depicts the recombination mechanism that gives form to the system and its interfaces. The saturation current, which in reverse bias provides the number of charges that may rise above the energetic barrier, is the second parameter that changes the exponential portion of *J*–*V* characteristics. The current–voltage dependency of the applied voltage junction according to thermionic emission can be written as [32–35],

$$I = I_s \left[\exp\left(\frac{qV}{nKT}\right) - 1 \right] \quad (V \geq 3k_B T/q) \quad (7)$$

The *I_s* is stated as the Eq. (8),

$$I_s = AA * T^2 \exp\left(-\frac{q\Phi_B}{KT}\right) \quad (8)$$

where *A*, *A**, and *Φ_B* denote the diode area, Richardson constant, and zero-bias barrier height. The ideality factor (*n*) can be determined during forwarding bias ln (*I*)–*V* plot from the straight-line region of the slope and can be written as Eq. (9) [35–37],

$$n = \frac{q}{KT} \frac{dV}{d(\ln I)} \quad (9)$$

Φ_B is determined by the following Eq. (10),

$$\Phi_B = \frac{KT}{q} \ln\left(\frac{AA * T^2}{I_0}\right) \quad (10)$$

The current intercept axis is used to measure the barrier height (*Φ_B*) and ideality factor (*n*) and the liner area slope of the forward-biased semi-log *J*–*V* curve and its respective values, which are described in Table 2. Individually, the n-Zr_xV₂O₅/p-Si diodes have lower ideality factor and barrier height values than the n-V₂O₅/p-Si diode. The resulting currents in these diodes are due to recombination and diffusion. The decrease in the element of ideality can be traced to the enhanced interface state of the doped diodes [38–40]. In addition, the V⁵⁺ lattice with Zr⁴⁺ ions reduces the number of oxygen vacancies. It results in a lower density of free carriers, which ultimately raises the height of interface barriers. Additionally,

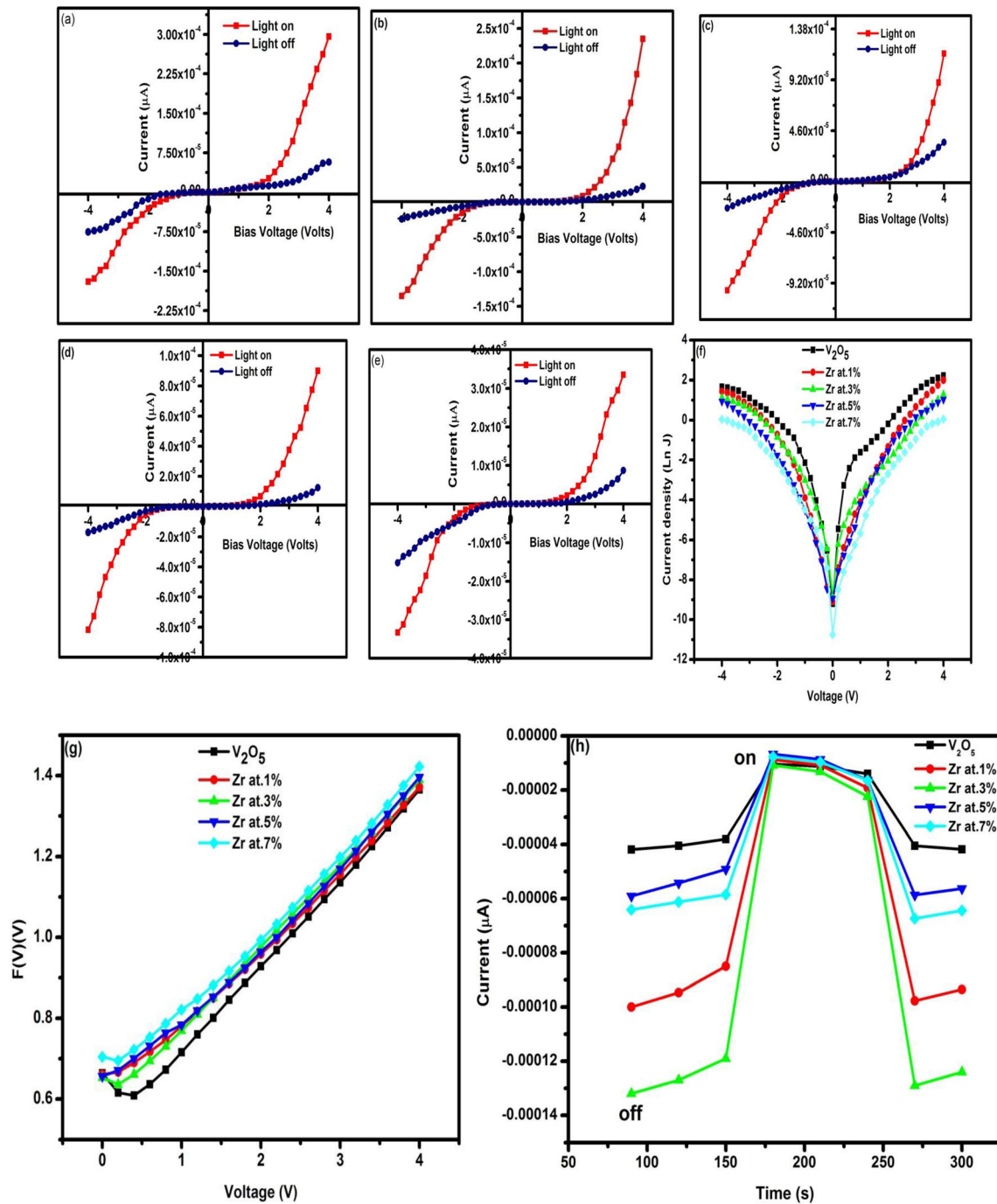


Fig. 12 **a–e** I – V characteristics of n- $Zr_xV_2O_5$ /p-Si diodes at the dark and light condition for various doping concentrations of Zr **a** 0, **b** 1, **c** 3, **d** 5, and **e** 7 wt%. **(f)** The $\ln J$ versus voltage

characteristics of n- $Zr_xV_2O_5$ /p-Si diodes, **g** $F(V)$ vs V plots of pure and n- $Zr_xV_2O_5$ /p-Si diodes, and **h** The time-resolved photocurrent of the n- $Zr_xV_2O_5$ /p-Si diodes

Norde used the following equations to determine the device's barrier height (Φ_B) and sequence resistance.

$$F(V) = \frac{V_o}{\gamma} - \frac{kT}{q} \left(\frac{I(V)}{A * AT^2} \right) \quad (11)$$

$$\phi_B = F(V_o) + \frac{V_o}{\gamma} - \frac{kT}{q} \quad (12)$$

$$R_s = \frac{kT(\gamma - n)}{qI_o} \quad (13)$$

Table 2 Electrical parameter of the developed device

$Zr_xV_2O_5$ (where $x = 1, 3, 5$ and 7%)	Band gap energy (eV)	Ideality factor (n)	Barrier height (Φ_B) (eV)	Saturation current (I_s) (μA)	Norde function	
					Φ_B (eV)	R_s (k Ω)
00	2.20	3.3949	0.4243	3.09×10^{-5}	0.4073	8.45×10^2
01	2.38	4.5943	0.3974	8.65×10^{-5}	0.3647	3.02×10^2
03	2.34	5.3266	0.4159	4.26×10^{-5}	0.3898	6.13×10^2
05	2.30	5.6609	0.4225	3.31×10^{-5}	0.4174	7.89×10^2
07	2.26	5.8043	0.4483	1.23×10^{-5}	0.4641	2.12×10^3

where $I(V)$ is the current value obtained from the I – V curve and γ is the first integer (dimensionless) greater than the ideality factor of the diode. $F(V_o)$ is the minimum point of $F(V)$ and V_o is the corresponding voltage. $F(V)$ vs. V plots for undoped and n- $Zr_xV_2O_5$ /p-Si diodes are shown in Fig. 12g, and the approximate values for both are described in Table 2. In this case, the difference between Norde and I – V values is noticeable. This is because high series resistance from the regular I – V plot might prevent the barrier heights' accurate evolution. A well-known technique for studying the transport system is time-dependent transient photocurrent measurements. Before the procedure, the system was kept in the dark for 15 min to keep the current at a steady application potential. After the stabilization time, the current is determined in the following sequence: 30 s in the dark, 30 s in the light. The junction diode's photo-sensing stability is performed regularly by the number of cycles by ON and OFF the lighting. Figure 12h shows the time-resolved photocurrent of the diodes produced. Since the photogenerated carriers are trapped at the bandgap states, the dark current is reduced due to thermal de-trapping of the trapped carriers. The current also returns to its original state due to the charging carriers' trapping in the dark at the deep depths. In addition, as the volume of Zr^{4+} content increases, the number of photocurrent increases compared to the undoped n- V_2O_5 /p-Si diode. As a result, photodiodes with varying amounts of Zr^{4+} are found to have a photoconduction action.

4 Conclusion

In summary, a series of Zr^{4+} -doped vanadium pentoxide nanorods were obtained using ammonium metavanadate as source material, using a one-step wet precipitation process. Zr-dopant increases crystallinity and homogeneity without impacting the host lattice V^{5+} main orthorhombic structure. SEM / TEM analyzes portray homogeneous nanorods for undoped V_2O_5 and their transition of surface morphology from nanorods to Zr-doping tetrapods. HR-TEM with SAED pattern exposing the single crystalline structure of V_2O_5 nanorods measured in (001) direction with a fringe width of ~ 0.43 nm. Raman and X-ray photoelectron spectroscopy tests show and examine that Zr's doping dimension has a lot of oxygen vacancies in the samples. Zr substitution allows the band difference to decrease considerably as compared to the pure V_2O_5 sample. The PL amplitude for the undoped V_2O_5 sample was found to be optimal, and Zr doping caused luminescence quenching. The electrical properties of the n- $Zr:V_2O_5$ /p-Si diode improved with increased Zr content due to increased charge carrier concentration and decreased defect condition in the V_2O_5 nanorods, as shown by the I – V characteristics and diode efficiency assessment. Also, we fabricated n- $Zr_xV_2O_5$ /p-Si designs that are considered future esteemed candidates for photoresponse activities. When devaluing the effect of Zr doping on the optoelectrical characteristics of the V_2O_5 nanorods, this finding can be refined and used as an appropriate candidate for the optoelectronic device application.

Acknowledgements

Authors wish to express their sincere thanks to the UGC-Rajiv Gandhi National Fellowship (F1-17.1/

2016-17/RGNF-2015-17-SC-TAM-8030) at New Delhi. Also, The authors express their gratitude to the Deanship of Scientific Research at King Khalid University for funding this work through research groups program under Grant number R.G.P. 2/137/42.

Data availability

The raw/processed data required to reproduce these findings cannot be shared at this time as the data also form part of an ongoing study.

Declarations

Conflict of interest The authors declare that they have no conflict of interest.

References

- R. Schlessler, R. Dalmau, D. Zhuang, R. Collazo, Z. Sitar, *J. Cryst. Growth* **281**, 75–80 (2005)
- L. Brewer, B.B. Ebbinghaus, *Thermochim. Acta* **129**, 49–55 (1988)
- Z. Guo, B. Liu, Q. Zhang, W. Deng, Y. Wang, Y. Yang, *Chem. Soc. Rev.* **43**, 3480–3524 (2014)
- Q. Song, H. Pang, W. Gong, G. Ning, S. Gao, X. Dong, C. Liu, J. Tian, Y. Lin, *RSC Adv.* **5**, 4256–4260 (2015)
- A. Cannavale, P. Cossari, G.E. Eperon, S. Colella, F. Fiorito, G. Gigli, H.J. Snaith, A. Listorti, *Energy Environ. Sci.* **9**, 2682–2719 (2016)
- S. Rafique, S.M. Abdullah, W.E. Mahmoud, A.A. Al-Ghamdi, K. Sulaiman, *RSC Adv.* **6**, 50043–50052 (2016)
- L. Minsu, S. Bin, Y. Tang, J. Xuchan, Y. Aibing, *Adv. Energy Mater.* **7**, 1700885 (2017)
- C. Julien, E. Haro-Poniatowski, M.A. Camacho-López, L. Escobar-Alarcón, J. Jíenez-Jarquín, *Mater. Sci. Eng. B* **65**, 170–176 (1999)
- M. Giorgetti, M. Berrettoni, W.H. Smyrl, *Chem. Mater.* **19**, 5991–6000 (2007)
- Y. Ji, D. Fang, C. Wang, Z. Zhou, Z. Luo, J. Huang, J. Yi, J. Alloy. *Compd.* **742**, 567–576 (2018)
- N. Singh, A. Umar, N. Singh, H. Fouad, O.Y. Allothman, F.Z. Haque, *Mater. Res. Bull.* **108**, 266–274 (2018)
- H. Song, C. Liu, C. Zhang, G. Cao, *Nano Energy* **22**, 1–10 (2016)
- A. Venkatesan, N.R. Krishna Chandar, A. Kandasamy, M. Karl Chinnu, K.N. Marimuthu, R. Mohan Kumar, R. Jayavel, *RSC Adv.* **5**, 21778–21785 (2015)
- I. Pradeep, E. Ranjith Kumar, N. Suriyanarayanan, K. Mohanraj, C. Srinivas, M.V.K. Mehar, *New J. Chem.* **42**, 4278–4288 (2018)
- V. Petkov, P.N. Trikalitis, E.S. Bozin, S.J.L. Billinge, T. Vogt, M.G. Kanatzidis, *J. Am. Chem. Soc.* **124**, 10157–10162 (2002)
- W. Yu, J. Wang, Z. Gou, W. Zeng, W. Guo, L. Lin, *Ceram. Int.* **39**, 2639–2643 (2013)
- B. Alonso, J. Livage, *J. Solid State Chem.* **148**, 16–19 (1999)
- C.J. Fontenot, J.W. Wiench, M. Pruski, G.L. Schrader, *J. Phys. Chem. B* **104**, 11622–11631 (2000)
- G.T. Chandrappa, P. Chithaiah, S. Ashoka, J. Livage, *Inorg. Chem.* **50**, 7421–7428 (2011)
- Y. Zhang, J. Zheng, Y. Zhao, T. Hu, Z. Gao, C. Meng, *Appl. Surf. Sci.* **377**, 385–393 (2016)
- M. Epifani, R. Díaz, C. Force, E. Comini, T. Andreu, R.R. Zamani, J. Arbiol, P. Siciliano, G. Faglia, J.R. Morante, *J. Phys. Chem. C* **117**, 20697–20705 (2013)
- X. Ren, Y. Jiang, P. Zhang, J. Liu, Q. Zhang, *J. Sol-Gel Sci. Technol.* **51**, 133–138 (2009)
- R. Baddour-Hadjean, M.B. Smirnov, K.S. Smirnov, V.Y. Kazimirov, J.M. Gallardo-Amores, U. Amador, M.E. Arroyo-de Dompablo, J.P. Pereira-Ramos, *Inorg. Chem.* **51**, 3194–3201 (2012)
- P. Clauws, J. Broeckx, J. Vennik, *Phys. status solidi* **131**, 459–473 (1985)
- S.-H. Lee, H.M. Cheong, M.J. Seong, P. Liu, C.E. Tracy, A. Mascarenhas, J.R. Pitts, S.K. Deb, *Solid State Ion.* **165**, 111–116 (2003)
- C.W. Zou, Y.F. Rao, A. Alyamani, W. Chu, M.J. Chen, D.A. Patterson, E.A.C. Emanuelsson, W. Gao, *Langmuir* **26**, 11615–11620 (2010)
- B.M. Reddy, B. Chowdhury, E.P. Reddy, A. Fernández, *J. Mol. Catal. A: Chem.* **162**, 431–441 (2000)
- S. Zhao, P. Li, Y. Wei, *Powder Technol.* **224**, 390–394 (2012)
- K. Karthika, K. Ravichandran, *J. Mater. Sci. Technol.* **31**, 1111–1117 (2015)
- L. Bixia, F. Zhuxi, J. Yunbo, *Appl. Phys. Lett.* **79**, 943–945 (2001)
- N.K. Dutta, R.J. Nelson, *J. Appl. Phys.* **53**, 74–92 (1998)
- P. Klason, M.M. Rahman, Q.-H. Hu, O. Nur, R. Turan, M. Willander, *Microelectron. J.* **40**, 706–710 (2009)
- A. Bengi, S. Altındal, S. Özçelik, S.T. Agaliyeva, T.S. Mammadov, *Vacuum* **83**, 276–281 (2009)
- O. Pakma, N. Serin, T. Serin, S. Altındal, *J. Sol-Gel Sci. Technol.* **50**, 28–34 (2009)
- A. Tataroglu, S. Altındal, *J. Alloy. Compd.* **479**, 893–897 (2009)
- O. Pakma, N. Serin, T. Serin, Ş Altındal, *J. Appl. Phys.* **104**, 014501 (2008)

37. M. Ozer, D.E. Yıldız, S. Altındal, M.M. Bulbu, Solid-State Electron. **51**, 941–949 (2007)
38. S. Altındal, H. Kanbur, D.E. Yıldız, M. Parlak, Appl. Surf. Sci. **253**, 5056–5061 (2007)
39. K. Mohanraj, D. Balasubramanian, J. Chandrasekaran, A. Chandra Bose, Mater. Sci. Semicond. Process. **79**, 74–91 (2018)
40. H.M. Zhang, W.C.H. Choy, IEEE Trans. Electron Devices **55**, 2517–2520 (2008)

Publisher's Note Springer Nature remains neutral with regard to jurisdictional claims in published maps and institutional affiliations.